Multifluid Modeling of the Desulfurization Process within a Bubbling Fluidized Bed Coal Gasifier

Lindsay-Marie Armstrong
Energy Technology Research Group, University of Southampton, Southampton SO17 1BJ, U.K.

Sai Gu
School of Engineering, Cranfield University, Cranfield, Bedfordshire MK43 0AL, U.K.

Kai H. Luo
Energy Technology Research Group, University of Southampton, Southampton SO17 1BJ, U.K.

Centre for Combustion Energy, Key Laboratory for Thermal Science and Power Engineering of Ministry of Education, Dept. of Thermal Engineering, Tsinghua University, Beijing 100084 China

Pinakeswar Mahanta
Dept. of Mechanical Engineering, Indian Institute of Technology Guwahati, Pin 781039, India

DOI 10.1002/aic.13997
Published online April 25, 2013 in Wiley Online Library (wileyonlinelibrary.com)

The desulfurization process to a two-dimensional (2-D) and three-dimensional (3-D) Eulerian–Eulerian computational fluid dynamic (CFD) model of a coal bubbling fluidized gasifier is introduced. The desulfurization process is important for the reduction of harmful SO_x emissions; therefore, the development of a CFD model capable of predicting chemical reactions involving desulfurization is key to the optimization of reactor designs and operating conditions. To model the process, one gaseous phase and five particulate phases are included. Devolatilization, heterogeneous, and homogeneous chemical reactions as well as calcination and desulfurization reactions are incorporated. A calcination-only model and a calcination plus desulfurization model are simulated in 2-D and 3-D and the concentrations of SO_2 leaving the reactors are compared. The simulated results are assessed against available published experimental data. The influence of the fluidized bed on the desulfurization is also considered. © 2013 American Institute of Chemical Engineers *AIChE J*, 59: 1952–1963, 2013
Keywords: bubble phenomena, coal (gasification, desulfurization), two fluid modeling

Introduction

Fluidized beds technologies (FBT) offer higher efficiencies over fixed-bed technologies as the fuel particles are suspended and mixed thoroughly allowing for good air-particle contact. The particles are small so the reaction rates are fast and the good mixing allows for complete carbon removal.

Computational fluid dynamic (CFD) is increasingly used for simulating the complex gas–solid flow processes that take place in FBT. Isothermal hydrodynamics modeling of fluidized beds has been used to enhance the understanding of complex interactions between gas and particles.[1–6] Computational models predicting the heat-transfer coefficient in bubbling fluidized beds have also been considered.[7–10]

For hydrodynamic and heat transfer, the Eulerian–Eulerian two-fluid model (TFM) is the most frequently applied method as it is less computationally exhaustive in comparison to the Eulerian–Lagrangian discrete method which simulates the individual particle dynamics compared to the TFM assumes the gas and solid phases as continuous and fully interpenetrating within each control volume. Interesting alternatives include a Lagrangian–Lagrangian approach[11–13] and a combination of the Eulerian–Eulerian continuum model and the Eulerian–Lagrangian discrete model.[14,15] However, these were limited to the number of particles due to computational costs. The multiphase-particle-in-cell method is a hybrid method, where particle properties are mapped to and from an Eulerian grid using interpolation functions.[16] A recent applications of this model include isothermal cases[17] and heat transport and chemical cases, including pyrolysis.[18,19]

The particulate phases are treated as a fluid with closure models accounting for particulate behaviors. The kinetic theory of granular flow (KTGF) is adopted to consider the particle motion. During random particle oscillations, inelastic collisions occur which dissipates energy. The granular temperature defines the average of the three variances of the particle's velocities due to these oscillations. A full mathematical description of the kinetic theory is provided in the literature.[20]

Reaction modeling is a recent development for simulating the gasification processes within fluidized beds and is still limited in scope due to the high-computational cost. However, the increase in computer performance and capabilities in recent years allows for such complex models to be carried out. A two-dimensional (2-D) Eulerian–Eulerian model of the gasification of Colombian coal was carried out[21] based on the experimental work from the literature.[22] Their model included

Correspondence concerning this article should be addressed to S. Gu at s.gu@cranfield.ac.uk.

the devolatilization, heterogeneous reactions, and homogeneous reactions and produced reasonable results. Their work was further extended to three-dimensions (3-D),[23] also obtaining reasonable results. However, their models considered a single solid phase for the coal and sand which is computationally more efficient but unrealistic, as different solid materials exhibit different material properties, for example, density, diameter, and so on. Separate phases for different solid phases have been carried out[24–26] and it was found that the use of multiple phases better represented the segregative tendencies of the bed due to different material properties.

Limestone calcination has been considered in fluidization modeling;[27,28] however, regardless of the multiphase flow dynamics being considered using semiempirical fluid-dynamic correlations, the model does not consider the complex gas-particle dynamics that are present. We previously introduced limestone calcination to an Eulerian–Eulerian CFD calculation.[25,26]

The release of SO_x and NO_x species, despite their low concentrations, is causing environmental problems. It is important to understand the factors that influence the production of such species, especially sulfur dioxide, SO_2. Several investigations have been performed on the detection of SO_x, NO_x, and the intermediates of their formations.[29–31] Several models have been performed to determine the release of low-concentration species during the devolatilization process[32,33] and also their inclusion in numerical models.[30,32,34] There are many factors that can affect the production of both SO_x and NO_x species including operating conditions and sorbents, such as limestone. Since Eulerian–Eulerian models have successfully been attempted to demonstrate the effects such modification have on the gasification processes in bubbling fluidized beds, it is important to use this type of modeling to expand into the regions of low-concentration modeling. Understanding the effects of low-concentration species such as SO_2, not only on the reactive behaviors within the bed and flow dynamics but also on the computational performance, are a stepping stone towards the inclusion of further low-concentration species, namely, their formation intermediates, which would then lead to a more realistic treatment of complex reactions.

The present article incorporates desulfurization modeling into the Eulerian–Eulerian TFM using multiple phases for coal, char, calcium carbonate ($CaCO_3$), calcium oxide (CaO), and calcium sulfate ($CaSO_4$). The desulfurization process, to the author's knowledge, has yet to be included in the Eulerian–Eulerian modeling of a bubbling fluidized bed gasifier. To incorporate the desulfurization process, additional gas species and reactions are required for species of much lower concentrations compared to those considered previously. The present article shows the influences such additions have on the computational performance, which has yet to be demonstrated, and is important before advanced devolatilization schemes can be considered. The effects of the concentration species on exiting emissions and the influence bed dynamics have on them are also considered.

Model Setup

The present numerical study includes five phases: one gaseous phase and five particulate phases, char, coal, $CaCO_3$, CaO, and $CaSO5_4$, within a fluidized bed with experimental measurements taken from the literature.[22] This model was chosen over the Eulerian–Lagrangian models as it is computationally more efficient in terms of computational time and memory. The commercial software ANSYS FLUENT 12.0 was used to simulate the multiphase model using the Eulerian–Eulerian multifluid model. This type of method allows for the presence of multiple phases in one control volume by introducing the volume fraction variable, a_i. Each of the solid phases restricts the granular particles to the same diameter and density as the properties are averaged over the control volumes and solved individually using the mass and momentum equations. The kinetic fluctuations between particles are considered using the KTGF. The virtual mass and lift effects are negligible as the lift only affects particles of large diameters and this is not the present case.

Conservation of mass

The conservation of mass for the gaseous and solid phases are modeled using the following equations

$$\frac{\partial(\alpha_g\rho_g)}{\partial t}+\nabla\cdot(\alpha_g\rho_g\vec{v}_g)=S_{gs} \tag{1}$$

$$\frac{\partial(\alpha_s\rho_s)}{\partial t}+\nabla\cdot(\alpha_s\rho_s\vec{v}_s)=S_{sg} \tag{2}$$

$$S_{sg}=-S_{gs}=w_i\Sigma Y_i R_i \tag{3}$$

where $\vec{v}_i$ and ρ_i represent the instantaneous velocity of the phase and density, respectively. A mass source term is introduced due to the mass, momentum, and heat exchange between the gaseous and solid phases as a result of the heterogeneous reactions. The gas density, ρ_g, is defined as a function of species composition and temperature using the ideal gas law, whereas the solid density, ρ_s, is defined by the composition of the species alone.

$$\rho_g=\frac{p}{RT\Sigma_{i=1}^{n}\frac{Y_i}{w_i}} \tag{4}$$

$$\rho_s=\frac{1}{\Sigma_{i=1}^{n}\frac{Y_i}{\rho_i}} \tag{5}$$

Conservation of momentum

The conservation of momentum equation for the gas and solid phases are given as follows

$$\frac{\partial(\alpha_g\rho_g\vec{v}_g)}{\partial t}+\nabla\cdot\left(\alpha_g\rho_g(\vec{v}_g\otimes\vec{v}_g)\right)=-\alpha_g\nabla p+\nabla\cdot\bar{\bar{\tau}}_g+\alpha_g\rho_g\vec{g}+K_{gs}(\vec{v}_g-\vec{v}_s)+S_{gs}\vec{v}_s \tag{6}$$

$$\frac{\partial(\alpha_s\rho_s\vec{v}_s)}{\partial t}+\nabla\cdot\left(\alpha_s\rho_s(\vec{v}_s\otimes\vec{v}_s)\right)=-\alpha_s\nabla p-\nabla p_s+\nabla\cdot\bar{\bar{\tau}}_s+\alpha_s\rho_g\vec{g}+K_{gs}(\vec{v}_g-\vec{v}_s)+S_{sg}\vec{v}_s \tag{7}$$

where K_{gs} and $\bar{\bar{\tau}}$ represent the interphase momentum transfer between the phases and the stress–strain tensor, respectively. The stress–strain tensors for the separate phases are given by

$$\bar{\bar{\tau}}_g=\alpha_g\mu_g(\nabla\vec{v}_g+\nabla\vec{v}_g^T)-\frac{2}{3}\alpha_g\mu_g(\nabla\cdot\vec{v}_g)\bar{\bar{I}}_g \tag{8}$$

$$\bar{\bar{\tau}}_s=\alpha_s\mu_s(\nabla\vec{v}_s+\nabla\vec{v}_s^T)+\alpha_s\left(\xi_s-\frac{2}{3}\mu_s\right)\nabla\cdot\vec{v}_s \tag{9}$$

where the bulk viscosity, ξ_s, accounts for the resistance of the particle to expansion and compression.[35] The gas viscosity, μ_g is made of the gas phase laminar viscosity and the gas phase turbulent viscosity

$$\xi_s = \frac{4}{3}\alpha_s d_s \rho_s g_0 (1+e)\left(\frac{\Theta_s}{\pi}\right)^{1/2} \quad (10)$$

$$\mu_g = \mu_{g_l} + \mu_{g_t} \quad (11)$$

The solid shear viscosity is composed of collisional, kinetic, and frictional effects. For the collisional and kinetic effects, the coefficient of restitution was introduced to account for the loss of energy due to particle collisions.[36] The coefficient quantifies the elasticity of the particle collisions, where a value of 0 is fully inelastic collisions, whereas a coefficient of 1 is a fully elastic collisions. Schaeffer's expression[37] is used to model the frictional viscosity in dense cases.

$$\mu_s = \mu_{s_{col}} + \mu_{s_{kin}} + \mu_{s_{fr}} \quad (12)$$

$$\mu_{s_{col}} = \frac{4}{5}\alpha_s d_s \rho_s g_0 (1+e)\left(\frac{\Theta_s}{\pi}\right)^{1/2} \quad (13)$$

$$\mu_{s_{kin}} = \frac{10 d_s \rho_s \sqrt{\Theta_s \pi}}{96\alpha_s (1+e) g_0}\left[1+\frac{4}{5}\alpha_s g_0 (1+e)\right]^2 \quad (14)$$

$$\mu_{s_{fr}} = \frac{p_s \sin\phi}{2\sqrt{I_{2D}}} \quad (15)$$

The solids pressure considers the kinetic effects and the effects due to particle collisions, and g_0 represents the radial distribution function which modifies the probability of particle collisions as the phase becomes dense

$$p_s = \alpha_s \rho_s \Theta_s + 2\rho_s (1+e)\alpha_s^2 g_0 \Theta_s \quad (16)$$

$$g_0 = \left[1-\left(\frac{\Sigma \alpha_{s_i}}{\alpha_{s_{max}}}\right)^{1/3}\right]^{-1} \quad (17)$$

The drag models represent the interphase momentum transfer between the gas and particle phases. The Gidaspow model[38] is a combination of the Wen and Yu model for dilute phases[39] and the Ergun model for dense phases[40]

$$K_{gs} = \begin{cases} 150\dfrac{\alpha_s^2 \mu_g}{\alpha_g d_s^2} + 1.75\dfrac{\alpha_s \rho_g |\vec{v_g} - \vec{v_s}|}{d_s} & \text{for } \alpha_g \le 0.8; \\ \dfrac{3}{4} C_D \dfrac{\alpha_g \rho_g |\vec{v_g} - \vec{v_s}|}{d_s}\alpha_g^{-2.65} & \text{for } \alpha_g > 08 \end{cases} \quad (18)$$

$$C_D = \begin{cases} \dfrac{24}{Re_s}[1+0.15Re_s^{0.687}] & \text{if } Re_s \le 1000; \\ 0.44 & \text{if } Re_s > 1000. \end{cases} \quad (19)$$

$$Re_s = \frac{\rho_g \alpha_g d_s |\vec{v_g} - \vec{v_s}|}{\mu_g} \quad (20)$$

The interphase exchange coefficient between the two solid phases, namely, limestone, s_1, and coal, s_2, was derived by Syamlal et al.[41]

$$K_{s_1 s_2} = \frac{3(1+e)\left(\frac{\pi}{2}\right)\alpha_{s_1}\alpha_{s_2}\rho_{s_1}\rho_{s_2}(d_{s_1}+d_{s_2})^2 g_0}{2\pi(\rho_{s_1} d_{s_1}^3 + \rho_{s_2} d_{s_2}^3)}|\vec{v_{s_1}} - \vec{v_{s_2}}| \quad (21)$$

Gas turbulence model

The $k-\varepsilon$ turbulence model is used to model the gaseous phase only. The solid phases are considered laminar due to the influence of drag in the bubbling bed dominating the solid flow behavior. The turbulent mixing rate and chemical kinetic rates are calculated for the finite-rate/eddy-dissipation homogeneous reaction model; therefore, it is important to consider a turbulent model for the gas phase. The transport equations for k and ε are as follows

$$\frac{\partial(\alpha_g \rho_g k)}{\partial t} + \nabla\cdot(\alpha_g \rho_g \vec{v_g} k) = \nabla\cdot\alpha_g\left(\mu_{gl} + \frac{\mu_{g_t}}{\sigma_k}\nabla\cdot k\right) + \alpha_g G_k - \alpha_g \rho_g \varepsilon \quad (22)$$

$$\frac{\partial(\alpha_g \rho_g \varepsilon)}{\partial t} + \nabla\cdot(\alpha_g \rho_g \vec{v_g} \varepsilon) = \nabla\cdot\alpha_g\left(\mu_{gl} + \frac{\mu_{g_t}}{\sigma_\varepsilon}\nabla\cdot\varepsilon\right) + \frac{\alpha_g \varepsilon}{\kappa}(C_{\varepsilon_1} G_\kappa - C_{\varepsilon_2}\rho_g \varepsilon) \quad (23)$$

$$\mu_{g_t} = \rho_g C_\mu \frac{k^2}{\varepsilon} \quad (24)$$

Eq. 24 defines the turbulence viscosity used in Eq. 9. The model constants are $C_{\varepsilon_1} = 1.44$, $C_{\varepsilon_2} = 1.92$, and $C_\mu = 0.09$. The turbulent Prandtl numbers for k and ε are $\sigma_k = 1.0$ and $\sigma_\varepsilon = 1.3$, respectively. G_k represents the generation of turbulent kinetic energy due to the mean velocity gradients and is represented by

$$G_k = -\rho_g \overline{v_i' v_j'}\frac{\partial v_j}{\partial x_i} \quad (25)$$

where

$$-\rho_g \overline{v_i' v_j'} = \mu_{g_t}\left(\frac{\partial v_i}{\partial x_j} + \frac{\partial v_j}{\partial x_i}\right) - \frac{2}{3}\rho_g k \delta_{ij} \quad (26)$$

KTGF

The granular temperature of the solid phases, Θ_s, is proportional to the kinetic energy of the random fluctuating motion of the particles. The following equation is solved for the granular temperature

$$\frac{3}{2}\left[\frac{\partial}{\partial t}(\alpha_s \rho_s \Theta_s) + \nabla\cdot(\alpha_s \rho_s \Theta_s)\right] = (-p_s\cdot\bar{\bar{I}} + \bar{\bar{\tau}}_s) : \nabla\vec{v}_s - \gamma_{\Theta_s} + \nabla\cdot(k_{\Theta_s}\cdot\nabla\Theta_s) - 3K_{gs}\Theta_s \quad (27)$$

The diffusion coefficient, k_{Θ_s}, and collisional dissipation, γ_{Θ_s}, are given by

$$k_{\Theta_s} = \frac{150\rho_s d_s\sqrt{\Theta_s \pi}}{384(1+e)g_0}\left[1+\frac{6}{5}\alpha_s g_0 (1+e)\right]^2 + 2\alpha_s^2 \rho_s d_s (1+e) g_0 \sqrt{\frac{\Theta_s}{\pi}} \quad (28)$$

$$\gamma_{\Theta_s} = \frac{12(1-e)^2 g_0}{d_s\sqrt{\pi}}\alpha_s^2 \rho_s \Theta_s^{3/2} \quad (29)$$

Conservation of energy

The conservation of energy considers the heat transfer within each phase and the exchange of heat between different phases. Each phase has a separate enthalpy equation and determined by the specific enthalpy, H, the thermal conductivity, λ_i, and the heat exchange between the gas and solid phases, Q_{gs}, as follows

$$\frac{\partial}{\partial t}(\alpha_g \rho_g H_g) + \nabla\cdot(\alpha_g \rho_g \vec{v}_g H_g) = \nabla(\lambda_g \nabla T_g) + Q_{gs} + S_{gs} H_s \quad (30)$$

$$\frac{\partial}{\partial t}(\alpha_s \rho_s H_s) + \nabla\cdot(\alpha_s \rho_s \vec{v}_s H_s) = \nabla(\lambda_s \nabla T_s) + Q_{sg} + S_{sg} H_s \quad (31)$$

Table 1. Heterogeneous, Homogeneous, Calcination, and Desulfurization Reactions with their Kinetic Rate Constants

	Heterogeneous	Kinetic rate constants	Reference
HT1	$C+O_2 \rightarrow CO_2$	$K_{Arr_1}=1.04\times10^5 T_c \exp\left(\frac{-11200}{T_c}\right)$	45,46
HT2	$C+H_2O \rightarrow CO+H_2$	$K_{Arr_2}=342 T_c \exp\left(\frac{-15600}{T_c}\right)$	45,46
HT3	$C+CO_2 \rightarrow 2CO$	$K_{Arr_3}=342 T_c \exp\left(\frac{-15600}{T_c}\right)$	45,46
HT4	$C+2H_2 \rightarrow CH_4$	$K_{Arr_4}=3.42\times10^{-3} \exp\left(\frac{-15600}{T_c}\right)$	45,46
	Homogeneous		
HM1	$CO+0.5O_2 \rightarrow CO_2$	$K_1=1.0\times10^{15} \exp\left(\frac{-16000}{T_g}\right) C_{CO} C_{O_2}^{0.5}$	28,47
HM2	$H_2+0.5O_2 \rightarrow H_2O$	$K_2=5.159\times10^{15} \exp\left(\frac{-3430}{T_g}\right) T^{-1.5} C_{H_2}^{1.5} C_{O_2}$	28,47
HM3	$CH_4+2O_2 \rightarrow 2H_2O+CO_2$	$K_3=3.552\times10^{14} \exp\left(\frac{-15700}{T_g}\right) T^{-1} C_{CH_4} C_{O_2}$	28,47
HM4	$CO+H_2O \Longleftrightarrow H_2+CO_2$	$K_4=2780 \exp\left(\frac{-1510}{T_g}\right)\left[C_{CO} C_{H_2O}-\frac{C_{CO_2} C_{H_2}}{0.0265\exp(3968/T_g)}\right]$	28,47
HM5	$4NH_3+5O_2 \rightarrow 4NO+6H_2O$	$K_5=9.78\times10^{11} \exp\left(\frac{-19655}{T_g}\right) C_{NH_3}^{0.86} C_{O_2}^{1.04}$	28,47
HM6	$2H_2S+3O_2 \rightarrow 2SO_2+2H_2O$	$K_6=9.78\times10^{11} \exp\left(\frac{-19655}{T_g}\right) C_{H_2S}^{0.86} C_{O_2}^{1.04}$	28,47
	Calcination		
CAL	$CaCO_3 \rightarrow CaO+CO_2$	$K_{cal}=122\exp(-4026/T_l)$	48
	Desulfurization		
DES	$CaO+SO_2+0.5O_2 \rightarrow CaSO_4$	$K_{ds}=470\exp(-881213/T_l) S_g \lambda_l$	50

$$H_s=\sum_j Y_i H_i \tag{32}$$

$$H_i=\int_{T_0}^{T} C_{p,i} dT+\Delta H_{f,i} \tag{33}$$

$$\lambda_g=\sum_j \frac{X_j \lambda_j}{\Sigma_j X_j \phi_{ij}} \tag{34}$$

where H_s represents the source term that includes sources of enthalpy, H_i is the enthalpy for each species in the mixture, and λ_g is the gas mixture thermal conductivity.

In Eq. 34, X_i represents the molar fraction of the ith species and $\phi_{ij}=\left[1+\left(\frac{\mu_i}{\mu_j}\right)^{1/2}\left(\frac{w_j}{w_i}\right)^{1/4}\right]/\left[8\left(1+\frac{w_i}{w_j}\right)\right]^{1/2}$.

The heat exchange between the phases, Q_{gs}, is a function of temperature difference and given by

$$Q_{gs}=-Q_{sg}=h_{gs}(T_g-T_s) \tag{35}$$

An empirical relation for the interphase heat-transfer coefficient between the gaseous and solid phases was proposed[42] which relates the Nusselt number with the particle Reynolds and the Prandtl numbers, $\mathrm{Pr}=\frac{C_{p,g}\mu_g}{\kappa_g}$

$$\mathrm{Nu_s}=(7-10\alpha_g+5\alpha_g^2)[1+07(\mathrm{Re_p})^{0.2}(\mathrm{Pr})^{1/3}]+(133-2.40\alpha_g+1.20\alpha_g^2)(\mathrm{Re_p})^{0.2}(\mathrm{Pr})^{1/3} \tag{36}$$

Species transport equations

The mass fraction of each species in the gas phase, Y_i is determined from the conservation equation of species transport as follows

$$\frac{\partial}{\partial t}(\alpha_g \rho_g Y_i)+\nabla(\alpha_g \rho_g \vec{v}_g Y_i)=-\nabla\cdot\alpha_g J_i+\alpha R_{g,i}+R_{s,i} \tag{37}$$

$$J_i=-\left(\rho_g D_{m,i}+\frac{\mu_t}{\mathrm{Sc_t}}\right)\nabla Y_i \tag{38}$$

$$D_{m,i}=\frac{1-X_i}{\Sigma_{j\neq i}\frac{X_j}{D_{i,j}}} \tag{39}$$

The second and third terms on the right-hand side of Eq. 37 represent the homogeneous rate of production of species, i, and the heterogeneous rate of reaction, respectively. J_i is the diffusion flux of the individual species, i, as a results of concentration gradients and is calculated using the modified Fick's law for the diffusion flux of chemical species in turbulent flow. $\mathrm{Sc_t}$ is the turbulent Schmidt number which is set to 0.7, and $D_{m,i}$ is the mixture diffusion coefficients.

Reaction modeling

The present article considers: (1) the coal devolatilization modeling; (2) heterogeneous char reactions, (3) homogeneous gaseous reactions, (4) limestone calcinations, and (5) desulfurization. The heterogeneous, homogeneous, calcination, and desulfurization reactions that take place are given in Table 1.

Devolatilization. During the devolatilization process, the coal phase immediately transfers the char into the char phase whilst the gaseous volatiles are released. For simplicity, the coal is assumed dry and ash free so the presence of ash is neglected in the present case. However, we are currently investigating the presence of ash with more complex reaction models.

$$\mathrm{Coal} \rightarrow \mathrm{Volatile}+\mathrm{Char} \tag{40}$$

$$\mathrm{Volatile} \rightarrow a_1CO_2+a_2CO+a_3CH_4+a_4H_2+a_5H_2O+a_6\mathrm{Tar}+a_7NH_3+a_8H_2S \tag{41}$$

The mass fraction, Y_i of the dominating volatile products released during devolatilization are determined using correlations that estimate the yields by the proximate analysis,[43] given in Table 2, as follows

Table 2. Characteristics of Solids

Coal properties					
Proximate analysis (wt %)					
Moisture	2.6				
Volatile matter	41.8				
Fixed carbon	54.1				
Ash	1.5				
Ultimate analysis (wt %)					
Carbon	75.3				
Hydrogen	5.4				
Oxygen	15.6				
Nitrogen	1.8				
Sulfur	0.4				
Ash	1.5				
Others	Coal	Char	$CaCO_3$	CaO	$CaSO_4$
Mean particle size (mm)	0.62	0.60	0.60	0.60	0.60
Apparent density (kg/m^3)	1250	450	2700	3320	2960
High heating value (kJ/kg)	29695				

$$Y_{CO_2}=0135-0900Y_{\text{volatile(daf)}}+1.906Y^2_{\text{volatile(daf)}} \quad (42)$$

$$Y_{CO}=0428-2653Y_{\text{volatile(daf)}}+4.845Y^2_{\text{volatile(daf)}} \quad (43)$$

$$Y_{CH_4}=0201-0469Y_{\text{volatile(daf)}}+0.241Y^2_{\text{volatile(daf)}} \quad (44)$$

$$Y_{H_2}=0157-0868Y_{\text{volatile(daf)}}+1.388Y^2_{\text{volatile(daf)}} \quad (45)$$

$$Y_{H_2O}=0409-2389Y_{\text{volatile(daf)}}+4.554Y^2_{\text{volatile(daf)}} \quad (46)$$

$$Y_{\text{Tar}}=-0325+7279Y_{\text{volatile(daf)}}-12.880Y^2_{\text{volatile(daf)}} \quad (47)$$

The volatile nitrogen and sulfur species are determined as a function of bed temperature, T,[44]

$$N=0001T-06(\text{kg/kg coal}) \quad (48)$$

$$S=0001T-006(\text{kg/kg coal}) \quad (49)$$

Heterogeneous Reactions. Heterogeneous reactions take place between the char and the surrounding gases. The char combustion between the char and O_2 takes place very quickly. The reactions take place on the external surface of the particles; therefore, models have been created that consider the kinetic, *K*–Arr, and the diffusive, *K*–Dif, rate constants as follows

$$R_C=\left((K_{\text{Arr}})^{-1}+(K_{\text{Dif}})^{-1}\right)C_{O_2} \quad (50)$$

$$K_{\text{Arr}}=AT_s^n\exp\left(\frac{E}{RT_s}\right) \quad (51)$$

$$K_{\text{Dif}}=\frac{ShD_{gs}w_C}{RT_sd_s} \quad (52)$$

$$\text{Sh}=20+06\text{Re}^{1/2}\text{Pr}^{1/3} \quad (53)$$

$$D_{gs}=\frac{8.34\times10^{-6}T^{1.75}}{p} \quad (54)$$

where Sh and D_{gs} are the Sherwood number and diffusion coefficient for the gas, respectively; C_{O_2} is the concentration of O_2; Re and Pr are the Reynolds and the Prandtl numbers, respectively; and A and E are the pre-exponential factors and activation energy, respectively.

The gasification heterogeneous reactions take place much slower than the combustion reaction and have a longer residence time within the bed. As a result, the reaction is not limited to only the external surface of the particle, therefore, the consideration of diffusion through the external surface does not need to be considered

$$R_C=K_{\text{Arr}}[C_g] \quad (55)$$

The kinetic rate constants ($kgm^{-3}s^{-1}$)[45,46] are provided in Table 1.

Homogeneous Reactions. The homogeneous reactions within the gaseous phase consider the effects of turbulent flow and chemical reactions. The kinetic rate constant, R_{Arr}, and the turbulent mixing rate constant, R_{Edd}, were calculated using the finite-rate/eddy-dissipation model within ANSYS FLUENT 12.0. The minimum of these two rates is then taken to be the net reaction rate.

$$R_{i,r}=\min(R_{\text{Arr}},R_{\text{Edd}}) \quad (56)$$

$$R_{\text{Arr}}=k_aT^zC_A^nC_B^m \quad (57)$$

$$R_{\text{Edd}}=4.0v'_{i,r}w_i\rho_g\frac{\varepsilon}{\kappa}\min\left[\min_R\left(\frac{Y_R}{v'_{R,r}w_R}\right),\frac{\Sigma_PY_P}{2\Sigma_j^Nv''_{j,r}w_j}\right] \quad (58)$$

where w_i is the species molecular weight and $v'_{i,r}$ and $v''_{j,r}$ are the stoichiometric coefficients. The homogeneous reactions with their kinetic rates ($kgm^{-3}s^{-1}$)[28,47] are provided in Table 1.

The Calcination Process. Limestone calcination is the breakdown of limestone, $CaCO_3$, into calcium oxide, CaO, and carbon dioxide, CO_2. The reaction proceeds only if the partial pressure of CO_2 is above the decomposition pressure of $CaCO_3$. The following equilibrium decomposition pressure[48] is used

$$P_{\text{eq}}=4.137\times10^7\exp(-20474/T_l) \quad (59)$$

The calcination rate proposed by Silcox et al.[48] is dependent on the temperature and partial pressures of CO_2 and is measured in $mol^{-2}s^{-1}$. Table 1 gives the reaction kinetics for K_{cal}

$$R_{\text{CAL}}=K_{\text{cal}}(P_{\text{eq}}-P_i) \quad (60)$$

There are several kinetic rates available for the limestone calcination process which range in complexity. This model does not account for the particle shrinkage or sintering effects as the Eulerian–Eulerian model is restricted to same size diameters for the $CaCO_3$ phase, and so on. A review of the calcination models and their complexities is available in the literature.[49]

The Desulfurization Process. The present article introduces the desulfurization reaction, where CaO produced during the calcination process reacts with SO_2, and O_2, to produce $CaSO_4$. The sulfation process only takes place in the outer layer of the CaO particle and stops once the pores become blocked with $CaSO_4$. An unreacted-core model was taken from the literature[50] which takes into account temperature, limestone reactivity, particle size, and gas concentrations. As with the calcination model, the particulate phase diameters will remain constant as a restriction of the Eulerian–Eulerian model.

$$R_D=(\pi/6)d_{\text{CaO}}^3K_{\text{ds}}C_{SO_2} \quad (61)$$

$$S_g=-384T_g+5.6\times10^4, \qquad T_g\geq1253K \quad (62)$$

$$S_g=35.9T_g-36.7\times10^4, \qquad T_g<1253K \quad (63)$$

Initial and boundary conditions

The model was set up according to an experimental study of Colombian coal.[22] Figure 1 displays a sketch of the model

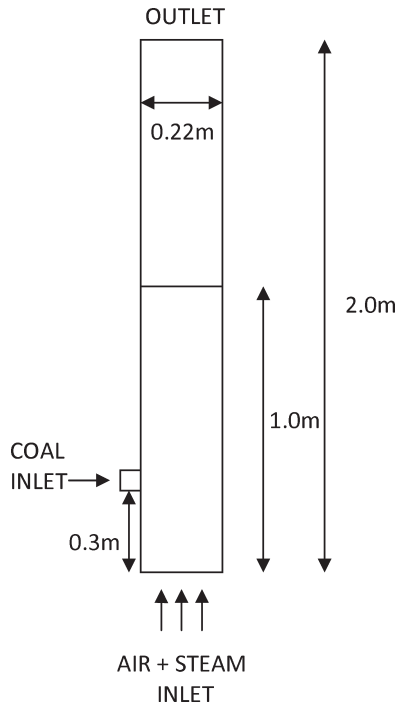

Figure 1. Schematic diagram of the experimental set up taken from the literature.[22]

set up used. The reactor had an internal diameter of 0.22 m and height of 2.0 m with a screw-feeder located at 0.3 m for the introduction of the coal and $CaCO_3$ mixture. An initial bed of calcium carbonate, $CaCO_3$, and char was set to the height of 1.0 m with a volume fraction of 0.48; an equal volume fraction was used for the two solid phases of 0.24 each. The diameter of the three limestone phases, namely, $CaCO_3$, CaO, and $CaSO_4$, have the same diameters but the densities vary according to the individual limestone constituent. The char is given as slightly smaller in diameter to the coal to allow for slight shrinkage following the devolatilization process. The initial gas composition was pure nitrogen, N_2 to prevent unwanted fast oxidation reactions taking place higher up the bed and the pressure outlet was fixed to an atmosphere. A more extensive description of the operating conditions can be found from the literature[22] but an overview of the present operating conditions and experimental results are given in Table 3.

The 2-D and 3-D meshes consisted of 2215 and 66,243 cells, respectively. As performed previously,[21,25,26,51] the 2-D cell size in the horizontal direction was 0.01 m whilst the vertical direction was set to 0.02 m creating a domain of (22 $\times$ 100) cells. A grid independence test was carried out for the 3-D case and found that increasing the horizontal cell size did not influence the results greatly. Furthermore, this agreed with previous findings which showed that doubling the overall 3-D cell size did not show significant differences in the solution.[52] Therefore, the 3-D case increased the horizontal cell size to 0.02 m but maintained the vertical cell size at 0.02 m. This was to reduce the computational exhaustivity. The region near the coal inlet was refined further to capture the devolatilization characteristics taking place. The wall boundary conditions for the gas phase were set to no-slip whilst the particulate phase had a tangential slip condition.[53]

Table 3. Operating Conditions and Experimental Results

Operating conditions		Experimental results	
Air (kg/h)	28.4	H_2 (%)	6.48
Steam (kg/h)	4.6	CO_2 (%)	14.86
Coal (kg/h)	8.0	N_2 (%)	71.54
Limestone (kg/h)	0.8	CH_4 (%)	1.29
Entrance temperature (K)	641.15	CO (%)	5.80
Reactor temperature (K)	1099.15		

Both the 2-D and 3-D simulations utilize six separate phases, a gaseous phase and five solid phases: coal, char, $CaCO_3$, CaO, and $CaSO_4$. To activate the desulfurization reaction, additional low-concentration species are required. The 2-D simulations consider the effects these low-concentration species and additional reactions have on the computational time. The base case, which was considered in our previous work,[25,26] implements a gaseous mixture of eight species, namely, H_2O, O_2, CO_2, CO, H_2, CH_4, tar, and N_2. As carried out by previous researchers,[21,54] the tar is regarded as C_6H_6 since the composition of tar is usually regarded as condensed nuclei aromatics. The cases are extended to determine the effects of additional gaseous species, NH_3 and H_2S alone on the computational time and also the addition of two homogeneous reactions and the products of such reactions, that is, NO and SO_2. Table 4 contains information about the three different cases with the various species and reactions considered.

Results

Effects on computational performance

The composition of the main exiting gases, set up with cases 1, 2, and 3, was averaged over a 50.0 s period, between 50.0 and 100.0 s, and compared with the experimental data from the literature,[22] and given in Figure 2. The main exiting emissions compare reasonably well with the experimental data but as expected additional gaseous species and reaction models do not greatly influence the main exiting emissions due to the low concentrations. This is due to the amount of nitrogen and sulfur species present in the coal being much low than the remaining species so the concentration of NH_3 and H_2S available for the additional reactions is very low in comparison.

The impact of the inclusion of additional species and reactions on the computational time is considered. The simulations were carried out on the supercomputer, IRIDIS 3 at the

Table 4. Two-Dimensional Cases with Varying Combinations of Gas Species and Reactions

Case	Gas species	No.
1	H_2O, O_2, CO_2, CO H_2, CH_4, C_6H_6, N_2	8
2	H_2O, O_2, CO_2, CO H_2, CH_4, C_6H_6, N_2, NH_3 H_2S	10
3	H_2O, O_2, CO_2, CO H_2, CH_4, C_6H_6, N_2, NH_3, H_2S, NO, SO_2	12
	Activated Homogeneous Reactions	
1	HM1, HM2, HM3, HM4	4
2	HM1, HM2, HM3, HM4	4
3	HM1, HM2, HM3, HM4, HM5, HM6	6
	Activated Heterogeneous Reactions	
1	HT1, HT2, HT3, HT4	4
2	HT1, HT2, HT3, HT4	4
3	HT1, HT2, HT3, HT4	4

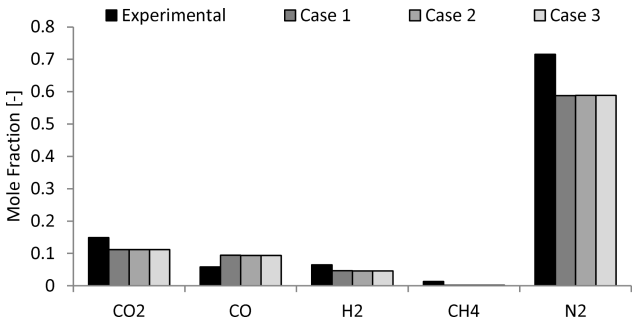

Figure 2. Comparison of cases 1, 2, and 3 with the experimental data taken from the literature.

University of Southampton. The maximum allocated time per session is a 60-h period; therefore, each case was allowed to run over four 60-h periods and the simulation times achieved during these periods are given in Figure 3. Increasing the number of gaseous species slows the simulations with an approximate delay of 1.5–2.0 s in the simulation times between Cases 1 and 2. Case 3 included an additional two gaseous species and also an additional two reactions which incurs a more pronounced delay in the simulation. This is due to the additional computational requirements needed to perform the simulations. Slight variations can be seen between the achieved simulation times particularly in cases 2 and 3, where the initial runs took slightly longer to perform. The amount of time to reach convergence of each iteration influences the times achieved during the runs. In cases 2 and 3, the bed contains very low-concentration species and additional slow reaction rates, which are lowest in the initial stages. As the concentration of these species accumulates the convergence time for the iterations improves.

Figure 4 compares the 2-D and 3-D results for case 3 with the experimental data. The results show minimal variation between the exiting emissions of the 2-D and 3-D cases. Since the 3-D cell sizes were increased to 0.02 m in the horizontal direction compared to 0.01 m in the 2-D case, this will likely reduce the accuracy of the results.

Calcination-only vs. desulfurization model

Two 3-D simulations were considered: one simulating the calcination process alone and the second including the desulfurization process. Figure 5 compares the average mole fraction of SO_2 leaving the reactor over a 100.0 s period,

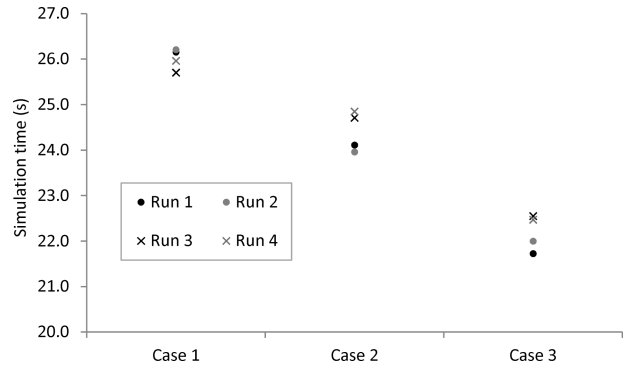

Figure 3. Simulation times (s) achieved during four 60-h periods for the different cases with varying numbers of species and reactions.

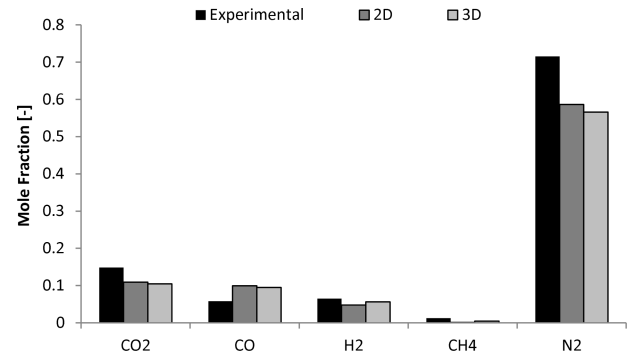

Figure 4. Comparison of 2D and 3D case 3 with the experimental data taken from the literature.

between 50.0 s and 150.0 s, for the calcination-only and calcination plus desulfurization model. As expected, there is a significant decrease in SO_2 emissions using the desulfurization model compared to the calcination-only model due to the consumption of SO_2 to form $CaSO_4$. The $CaSO_4$ distribution within the reactor, Figure 6, occupies the lower bed, where O_2 concentrations are high to promote the desulfurization reaction. We previously demonstrated that the presence of multiple phases can produce segregation effects due to the different fluid properties.[25,26] Whilst the high density of $CaSO_4$, compared to the char, would result in the segregation of the $CaSO_4$, which is why lower $CaSO_4$ volume fractions

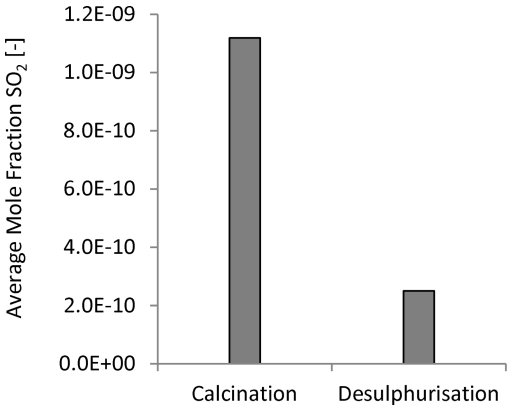

Figure 5. Average mole fraction of SO_2 over a 100.0 s period for the calcination-only and desulfurization model.

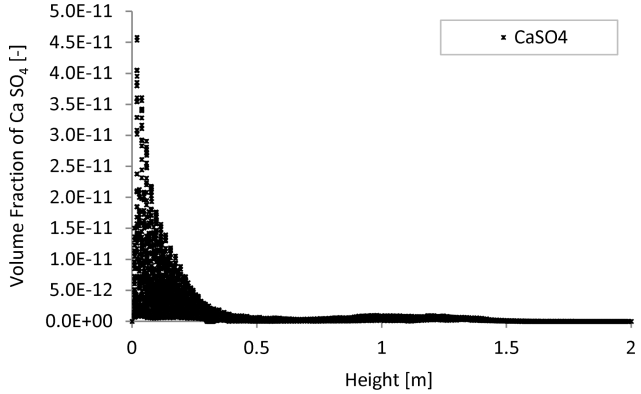

Figure 6. Volume fraction of $CaSO_4$ throughout the reactor.

Table 5. SO_2 yields Comparing a Simulated Bed of Coal Against Experimental Data from the Literature[30]

Case	Mole fraction of SO_2
Present case	6.157710^{-3}
Published case	$\approx 9.7710^{-3}$

are observed higher in the bed despite the mixing behavior of the bed. Furthermore, the increased temperatures near the air inlet would greatly influence the high-volume fraction of $CaSO_4$ in lower regions since the higher temperatures increase the desulfurization reaction rate, therefore, producing higher concentrations locally.

The low-volume fraction of the $CaSO_4$ is due to the limited availability of the reactant, SO_2. Both the calcination-only and the desulfurization cases, the mole fraction of SO_2 is very low, because the bed consists of char and $CaCO_3$ alone with the coal being introduced through the fuel inlet only. Therefore, the overall amount of sulfur which is released is collectively very low. To make a comparison with experimental data, the simulation is rerun with coal present, $a_{coal} = 0.1$, within the bed, in addition to its introduction through the fuel inlet. The experiments of Norman et al.[30] were performed in excess of 500.0–600.0 s as this was the time required for the SO_2 to reach a form of steady-state. The present article performed the coal bed simulation to 800.0 s as we previously demonstrated that steady-state conditions were achieved after approximately 400.0–500.0 s on a 2-D calcination-only case.[26] The average mole fraction of SO_2 leaving the reactor are compared with the experimental data[30] in Table 5. The mole fraction of SO_2 has greatly increased compared to the present benchmark due to the increased coal presence within the bed. A similar order of magnitude to the experimental data is observed but variations in set up and operating conditions lead to an expected variation in overall value.

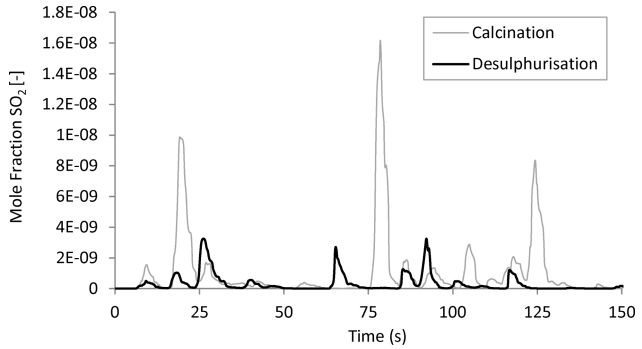

Figure 7. Mole fraction of SO_2 leaving the reactor using a calcination-only model and a model with desulfurization.

Influences on SO_2 production

The average mole fractions of exiting SO_2 were tracked over a 150.0 s period and shown in Figure 7. High peaks occur as large collections of SO_2 leave the reactor. This is especially seen in the calcination-only model around 20.0, 80.0, and 125.0 s. Peaks occur for the desulfurization model but with a lower mole fraction due to SO_2 consumption. SO_2 is produced during the oxidation of H_2S so an increase in either the local temperature or concentration of any of the reactants, H_2S or O_2, could be responsible for these peaks. Figure 8 plots the mole fractions of SO_2, O_2, H_2S and the temperature distribution at 73.5 s and 74.0 s at height $y = 0.03$ m for the calcination-only model. An increase in SO_2 occurs between this period prior to the peak observed at 80.0 s in Figure 7. The changes in temperature and O_2 distributions between the two time periods are negligible but there is an increase in H_2S which is responsible for the dramatic increase in SO_2.

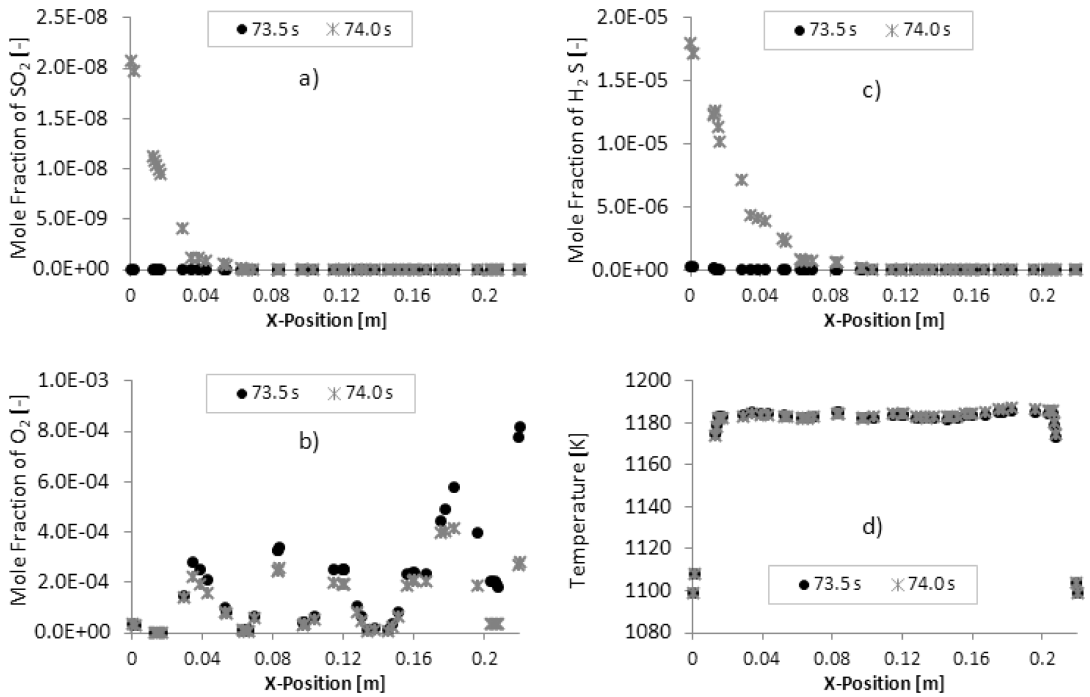

Figure 8. Mole fraction distributions of (a) SO_2, (b) O_2, (c) H_2S, and (d) the temperature distribution across the reactor at $y = 0.03$ m at 73.5 s and 74.0 s.

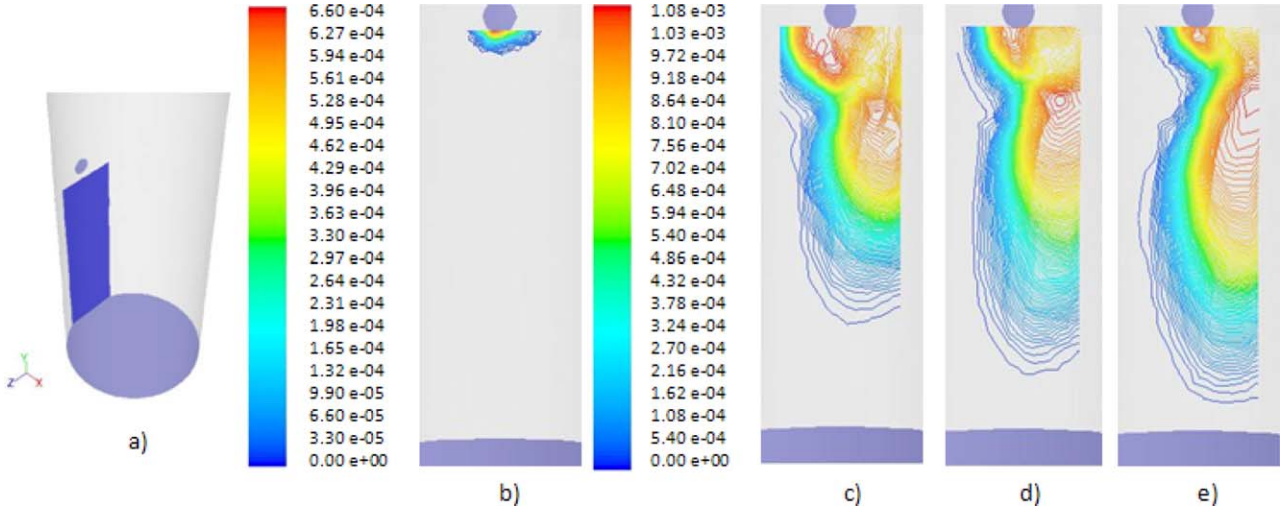

Figure 9. Mole fraction of H_2S shown across the (a) plane sliced at $x = 0.01$ m up to $y = 0.3$ m at the times (b) 72.00 s, (c) 73.50 s, (d) 73.75 s, and (e) 74.0 s.

[Color figure can be viewed in the online issue, which is available at wileyonlinelibrary.com.]

The increase in H_2S could be due to numerical errors but it is worth considering the bed behavior during this time period to be more conclusive. Figure 9 displays the contours of the mole fraction of H_2S across a plane (displayed in Figure 9a) at $x = 0.01$ m which spans between $y = 0$ m and $y = 0.3$ m at 72.00, 73.50, 73.75, and 74.00 s. The H_2S descends towards the air/steam inlet, where O_2 is prevalent, thus accelerating reaction HM6, producing additional SO_2.

Figure 10a–c displays iso-surfaces of the gas with a volume fraction of 0.75 at the times 72.00, 73.00, and 74.00 s.

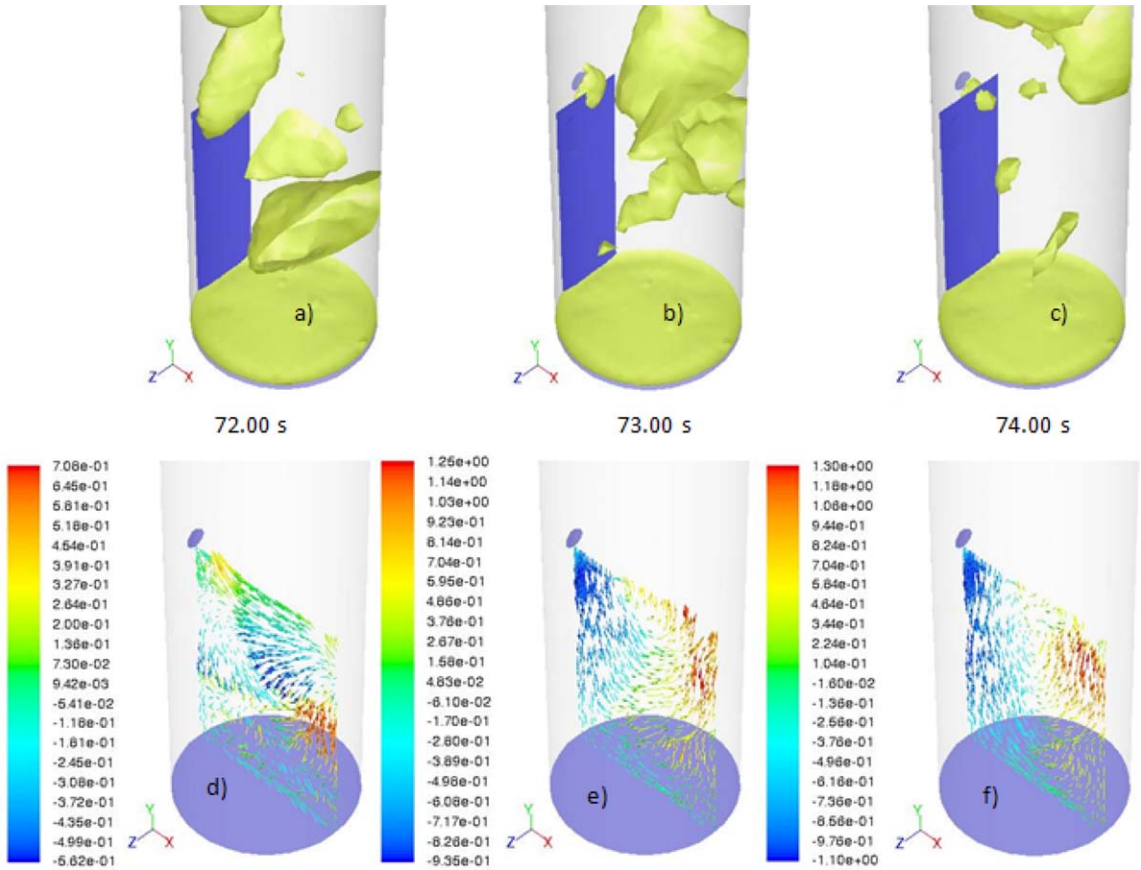

Figure 10. Iso-surface with gas volume fraction set to 0.75 (a–c) and the *y*-direction velocity distribution for the solids (d–f) at 72.00 s, 73.00 s, and 74.00 s, respectively.

[Color figure can be viewed in the online issue, which is available at wileyonlinelibrary.com.]

Previously at 72.00 s, in Figure 9b, the H_2S resided near the coal inlet. It is clear from Figure 10a, this is due to the large bubble formation build up from devolatilization products, including H_2S. The large bubble in the lower region was endogenously formed from the products of the heterogeneous reactions that dominate the lower bed regions. As the lower bubble rises, it coalesces with the bubble near the coal inlet and continues up the bed, as shown at 73.00 s in Figure 10b, c. Devolatilization products form a new bubble near the coal region, however, a slight downward tendency is apparent at 74.00 s.

The *y*-direction velocity distributions of the solid particles in Figure 10d–f show faster upward motion occurs in bubble regions where bed resistance is low. This explains why the H_2S remains high, near the coal inlet at 72.00 s, as the velocity vectors, in Figure 10d, have a positive velocity (indicating an upward direction) into the bubble. The velocities at 73.00 s and 74.00 s (Figure 10d, e) display a strong downward motion transporting the local solids and gases, that is, devolatilization products, towards the base of the reactor. This downward motion occurs as the bed occupies the voidage left by the ascending bubbles. The motion of the bed greatly influences the reactions as the bed aids the transport of the reactants to areas where the reactions dominate, such as oxidation reactions near the air inlet.

Conclusion

A CFD model for a bubbling bed coal gasifier has been developed using one gaseous phase and five particulate phases. Compared to previous models which incorporated all the solid materials as a single phase, this model has demonstrated realistic segregation effects due to the different properties.[25,26] The inclusion of chemical reactions into an Eulerian–Eulerian framework is recent due to its complexity. The different stages of gasification were considered, namely, devolatilization, heterogeneous and homogeneous reactions, and limestone calcination between different phases. The desulfurization process was also introduced to determine the model's capability of simulating low concentrations of species.

Assumptions are regularly made in CFD modeling regarding the accuracy of the chemical models and balancing acts are carried out between the inclusion of more detailed species to improve results and computational time/expense. The present results show that the inclusion of low-concentration nitrogen and sulfur based species does not affect the emissions of the major species leaving the reactor as nitrogen and sulfur concentrations are so small in comparison to the major species. However, the CFD predictions of the major species agree well with the experimental data.

The inclusion of additional species and reactions incurs a computational overhead. Conversely, the inclusion of sulfur and nitrogen in computational models is important as current research focuses on the reduction of SO_x and NO_x emissions to meet regulations. The present article shows that it is possible to carry out an Eulerian–Eulerian CFD model for multiple gaseous species with the newly incorporated reaction modeling for calcination and/or desulfurization for fluidized bed technologies to aid future design optimization.

3-D simulations were performed comparing SO_2 emissions from the calcination-only model and the calcination plus desulfurization model. The average mole fraction of SO_2 leaving the reactor showed a decrease, as expected, using the desulfurization model due to the additional consumption of SO_2. Occasional high peaks of SO_2 were observed for both the calcination-only and the desulfurization model, greater for the calcination-only case. This was due to the mixing behavior of the fluidized bed distributing concentrated collections of reactants to higher temperature regions, thus accelerating the production of SO_2. The occurrence frequencies and magnitudes of the peaks vary for both the calcination-only and calcination plus desulfurization models, which indicate complex flow and reaction dynamics in the fluidized beds.

Future applications as a result of this article include the use of more accurate yield predictions for low-concentration species and additional reactions between intermediate reactants to provide analyze of NO_x and SO_x formation in greater depth.

Notation

Greek letters

a_i = volume fraction
γ_i = collisional dissipation of energy, W/mK
κ = turbulent kinetic energy, m^2/s^2
λ_i = thermal conductivity of species, W/m^2K
μ_i = shear viscosity, kg/s m
ϕ = angle of internal friction, °, Eq. 15
ρ_i = density, kg/m^3
σ_κ = turbulent Prandtl numbers for κ
σ_ε = turbulent Prandtl numbers for ε
τ_i = stress tensor, Pa
Θ_s = particle phase pseudo-temperature, m/s^2
υ_i = velocity, m/s
ε = dissipation rate of turbulent kinetic energy, m^2/s^2
ξ_i = bulk viscosity, kg/s m

Symbols

t = time, s
I_i = stress tensor, Pa
C_D = drag coefficient
C_i = concentration of species *i*, $kmol/m^3$
C_p = specific heat, J/kgK
d_s = particle diameter, m
D_i = diffusion coefficient for species, m^2/s
e = coefficient of restitution
g = gravity, m/s^2
g_0 = radial distribution function
G_k = shear production
H = specific enthalpy, J/kg
h = heat-transfer coefficient, W/m^2K
J_i = diffusion flux if species *i*, kg/m^2s
k_{Θ_s} = diffusion coefficient for granular energy, kg/ms
K_{Arr} = kinetic rate constant
K_{Dif} = diffusion rate constant
K_i = drag, kg/m^3s
p = gas pressure, Pa
p_i = phase pressure, Pa
Q_i = intensity of heat exchange between phases, W/m^2
R = universal gas constant, J/kmol K
$R_{g,i}$ = net rate of production of homogeneous species *i*
$R_{s,i}$ = heterogeneous reaction rate
S_i = mass source term, kg/m^3s
T = temperature, K
w_i = species molecular weight, kg/kmol
X_i = molar fraction of species
Y_i = mass fraction of species

Subscripts

g = gas phase
i = general index, *i*th species
q = phase
s = solid phase
w = wall

c = char
g_l = gas laminar flow
g_t = gas turbulent flow

Dimensionless numbers

Nu = Nusselt number
Pr = Prandtl number
Re = Reynolds number
Sc_t = Turbulent Schmidt number
Sh = Sherwood number

Acknowledgments

The authors gratefully acknowledge the financial support from UK EPSRC Grant EP/G034281/1, and EU FP7 iComFluid Project (Grant No. 312261).

Literature Cited

1. Berruti F, Chaouki J, Godfroy L, Pugsley T, Patience G. Hydrodynamics of circulating fluidized bed risers: a review. *Can J Chem Eng*. 1995;73(5):579–602.
2. Samuelsberg A, Hjertager B. An experimental and numerical study of flow patterns in a circulating fluidized bed reactor. *Int J Multiphase Flow* 1995;22:575–591.
3. Benyahia S, Arastoopour H, Knowlton T, Massah H. Simulation of particles and gas flow behaviour in the riser section of a circulating fluidized bed using the kinetic theory approach for the particulate phase. *Powder Technol*. 2000;112:24–33.
4. Almuttahar A, Taghipour F. Computational fluid dynamics of high density circulating fluidized bed riser: study of modeling parameters. *Powder Technol*. 2008;185:11–23.
5. Goldschmidt M, Kuipers J, van Swaaij W. Hydrodynamic modelling of dense gas-fluidized beds using the kinetic theory of granular flow: effect of restitution coefficient on bed dynamics. *Chem Eng Sci*. 2001;56:571–578.
6. Armstrong LM, Luo K, Gu S. Two-dimensional and three-dimensional computational studies of hydrodynamics in the transition from bubbling to circulating fluidised bed. *Chem Eng J*. 2010a;160:239–248.
7. Patil D, Smit J, van Sint Annaland M, Kuipers J. Wall-to-bed heat transfer in gas-solid bubbling fluidized beds. *AIChE J*. 2006;52:58–74.
8. Schmidt A, Renz U. Numerical prediction of heat transfer in fluidized beds by a kinetic theory of granular flows. *Int J Therm Sci*. 2000;39:871–885.
9. Kuipers J, Prins W, van Swaaij W. Numerical calculation of wall-to-bed heat transfer coefficients in gas-fluidized beds. *AIChE J*. 1992;38:1079–1091.
10. Armstrong LM, Gu S, Luo K. The influence of multiple tubes on the tube-to-bed heat transfer in a fluidised bed. *Int J Multiphase Flow*. 2010;36(11-12):916–929.
11. Ge W, Li J. Pseudo-particle approach to hydrodynamics of gas/solid two-phase flow. In Proceedings of the 5th International Conference on Circulating Fluidized Beds. Beijing: Science Press, 1997:260–265.
12. Ge W, Li J. Macro-scale pseudo-particle modeling for particle-fluid systems. *Chin Sci Bulletin*. 2001;46(18):1503–1507.
13. Ge W, Li J. Macroscale phenomena reproduced in microscopic systems-pseudo-particle modeling of fluidization. *Chem Eng Sci*. 2003;58:1565–1585.
14. Papadikis K, Bridgwater A, Gu S. CFD modelling of the fast pyrolysis of biomass in fluidised bed reactors, part a: Eulerian computation of momentum transport in bubbling fluidised beds. *Chem Eng Sci*. 2008;63(16):4218–4227.
15. Papadikis K, Gu S, Bridgwater A. CFD modelling of the fast pyrolysis of biomass in fluidised bed reactors. part b: heat, momentum and mass transport in bubbling fluidised beds. *Chem Eng Sci*. 2009;64:1036–1045.
16. Andrews M, O'Rourke P. The multiphase particle-in-cell (mp-pic) method for dense particulate flows. *Int J Multiphase Flow*. 1996;22:379–402.
17. Snider D. An incompressible three-dimensional multiphase particle-in-cell model for dense particle flows. *J Comput Phys*. 2001;170:523–549.
18. O'Rourke P, Zhao P, Snider D. A model for collisional exchange in gas/liquid/solid fluidized beds. *Chem Eng Sci*. 2009;64:1784–1797.
19. Snider D, Clark S, O'Rourke P. Eulerian–Lagrangian method for three-dimensional thermal reacting flow with application to coal gasifiers. *Chem Eng Sci*. 2011;66:1285–1295.
20. Gidaspow D. Multiphase Flow and Fluidization, Continuum and Kinetic Theory Descriptions. London: Academic Press, Inc., 1994.
21. Yu L, Lu J, Zhang X, Zhang S. Numerical simulation of the bubbling fluidized bed coal gasification by the kinetic theory of granular flow (KTGF). *Fuel*. 2007;86:722–734.
22. Ocampo A, Arenas E, Chejne F, Espinel J, Londono C, Aguirre J, Perez J. An experimental study on gasification of Colombian coal in fluidised bed. *Fuel*. 2003;82:161–164.
23. Wang X, Jin B, Zhong W. Three-dimensional simulation of fluidized bed coal gasification. *Chem Eng Proc*. 2009;48:695–705.
24. Gerber S, Behrendt F, Oevermann M. An Eulerian modeling approach of wood gasification in a bubbling fluidized bed reactor using char as bed material. *Fuel*. 2010;89(10):2903–2917.
25. Armstrong LM, Luo K, Gu S. Effects of limestone calcination on the gasification processes in a BFB coal gasifier. *Chem Eng J*. 2011a;168:848–860. doi:10.1016/j.cej.2011.01.102.
26. Armstrong LM, Luo K, Gu S. A parametric study of the gasification processes in a BFB coal gasifier. *Ind Eng Chem Res*. 2011b;50:5959–5974.
27. de Souza-Santos M. Comprehensive modeling and simulation of fluidized bed boilers and gasifiers. *Fuel*. 1989;68:1507–1521.
28. Chejne F, Hernandez J. Modeling and simulation of coal gasification process in fluidized bed. *Fuel*. 2002;81:1687–1702.
29. Jones J, Harding A, Brown S, Thomas K. Detection of reactive intermediate nitrogen and sulfur species in the combustion of carbons that are models for coal chars. *Carbon* 1995;33:833–843.
30. Norman J, Pourkashanian M, Williams A. Modelling the formation and emission of environmentally unfriendly coal species in some gasification processes. *Fuel*. 1997;76:1201–1216.
31. Shimizu T, Satoh M, Fujikawa T, Tonsho M, Inagaki M. Simultaneous reduction of so_2, no_x and n_2o emissions from a two-stage bubbling fluidized bed combustor. *Energy Fuels*. 2000;14:862–868.
32. Ma R, Felder R, Ferrell J. Evolution of hydrogen sulfide in a fluidized bed coal gasification reactor. *Ind Eng Chem Res*. 1989;28:27–33.
33. Goyal A, Rehmat A. Modeling of a fluidised bed coal carbonizer. *Ind Eng Chem Res*. 1993;32:1396–1410.
34. Lin W, Bu J, Korbee R, Svoboda K, van den Bleek C. Modelling so_2 and no_x emissions in fluidized bed combustion of coal. *Fuel*. 1993;72:299–304.
35. Lun C, Savage S, Jeffrey D, Chepurniy N. Kinetic theories for granular flow: inelastic particles in Couette flow and slightly inelastic particles in a general flow field. *J Fluid Mech*. 1984;140:223–256.
36. Jenkins J, Savage S. A theory for the rapid flow of identical, smooth, nearly elastic, spherical particles. *J Fluid Mech*. 1983;130:187–202.
37. Schaeffer D. Instability in the evolution equations describing incompressible granular flow. *J Diff Equ*. 1987;66:19–50.
38. Gidaspow D, Bezburuah R, Ding J. Hydrodynamics of circulating fluidized beds: kinetic theory approach. In: Proceedings of the 7th International Conference on Fluidization, Gold Coast, Australia, May 3-8, 1992.
39. Wen Y, Yu Y. Mechanics of fluidization. *Chem Eng Prog Symp Ser*. 1966;62:100–111.
40. Ergun, S. Fluid flow through packed columns. *Chem Eng Prog*. 1952;48(2):89–94.
41. Syamlal M, O'Brien T. Derivation of a drag coefficient from velocity-voidage correlation. In: U.S. Dept. of Energy, Office of Fossil Energy, National Energy Technology Laboratory. Morgantown, West Virginia, April. 1987.
42. Gunn D. Transfer of heat or mass to particles in fixed and fluidised beds. *Int J Heat Mass Transfer*. 1978;21:467–476.
43. Loison R, Chauvin R. Pyrolise rapide du charbon. *Chimie et Industrie* 1964;91:260–275.
44. Fine D, Slater S, Sarofim A, Williams G. Nitrogen in coal as a source of nitrogen oxide emission from furnaces. *Fuel*. 1974;53:120–128.
45. Ross I, Davidson J. The combustion of carbon particles in a fluidized bed. *Chem Eng Res Des*. 1982;60a:108–114.
46. Hobbs M, Radulovic P, Smoot L. Modeling fixed-bed coal gasifiers. *AIChE J*. 1992;38:681–702.
47. Hurt R, Calo J. Semi-global intrinsic for char combustion modeling. *Combust Flame*. 2001;125:1138–2114.
48. Silcox G, Kramlich J, Pershing D. A mathematical model for the flash calcination of dispersed $caco_3$ and $ca(oh)_2$ particles. *Ind Eng Chem Res*. 1989;28:155–160.

49. Stanmore B, Gilot P. Review calcination and carbonation of limestone during thermal cycling for co_2 sequestration. *Fuel Proc Tech.* 2005;86:1707–1743.
50. Adanez J, Gayan P, Grasa G, deDiego L, Armesto L, Cabanillas A. Circulating fluidized bed combustion in the turbulent regime: modelling of carbon combustion efficiency and sulphur retention. *Fuel.* 2001;80:1405–1414.
51. Enwald H, Peirano E, Almstedt A, Leckner B. Simulation of the fluid dynamics of a bubbling fluidized bed experimental validation of the two-fluid model and evaluation of a parallel multiblock solver. *Chem Eng Sci.* 1999;54:311–328.
52. Xie N, Battaglia F, Pannala S. Effects of using two- verses three-dimensional computational modeling of fluidized beds. Part i, hydrodynamics. *Powder Technol.* 2008;182:1–13.
53. Johnson P, Jackson R. Frictional-collisional constitutive relations for granular materials, with application to plane shearing. *J Fluid Mech.* 1987;176:67–93.
54. Petersen I, Werther J. Experimental investigation and modeling of gasification of sewage sludge in the circulating fluidized bed. *Chem Eng Proc.* 2005;44(7):717–736.

Manuscript received Jun. 12, 2012, and revision received Nov. 21, 2012.